Oxidation Characteristics of Ti-14Al-21Nb Alloy

Sankara N. Sankaran,
Ronald K. Clark,
Jalaiah Unnam,
and Karl E. Wiedemann

NASA

Oxidation Characteristics
of Ti-14Al-21Nb Alloy

Sankara N. Sankaran
Analytical Services & Materials, Inc.
Hampton, Virginia

Ronald K. Clark
Langley Research Center
Hampton, Virginia

Jalaiah Unnam
and Karl E. Wiedemann
Analytical Services & Materials, Inc.
Hampton, Virginia

Summary

The static oxidation kinetics of Ti-14Al-21Nb (percent weight) ingot alloy were studied in air over the temperature range from 649°C to 1093°C in a thermogravimetric apparatus. The oxidation products were characterized by X-ray diffraction, electron microprobe analysis, energy dispersive X-ray analysis, and Auger electron spectroscopy. Cross sections of the oxidized samples were also examined using light and scanning electron microscopy. The oxidation rate was substantially lower than the conventional alloys of titanium, but the kinetics displayed a complex behavior involving two or more oxidation rates depending on the temperature and duration of exposure. The primary oxide formed was TiO_2, but this oxide was doped with Nb. Small amounts of Al_2O_3 and TiN were also present in the scale. The diffusion of oxygen into the alloy was observed, and the diffusivity seemed to be dependent on the microstructure of the metal. A model has been presented to explain the oxidation behavior of the alloy in terms of the reduction in the oxygen diffusivity in the oxide caused by the modification of the defect structure of TiO_2 by Nb ions.

Introduction

Titanium aluminides are candidate materials for use in hypersonic structures because of their high specific strength and superior high-temperature properties compared with conventional titanium alloys and superalloys. These exceptional properties are the result of the ordered microstructure. However, like most intermetallics, these alloys suffer from a lack of adequate room-temperature ductility. Variations in composition through the addition of other elements such as niobium, vanadium, and molybdenum are being attempted to overcome this problem. The alloy Ti-14Al-21Nb (percent weight) is one such modification of the intermetallic Ti_3Al in which Nb has been added to improve the room-temperature ductility.

Hypersonic structures are expected to be exposed at high temperatures to a variety of environments including oxygen, and thus oxidation resistance of the candidate alloys is of importance. Although some mechanistic studies on the role of aluminum and niobium on the oxidation of titanium have been reported (refs. 1-5), only a few limited studies (refs. 6 and 7) on the oxidation behavior of titanium aluminides have appeared in the open literature. The purpose of the present study was, therefore, to characterize the oxidation behavior of Ti-14Al-21Nb ingot alloy.

The oxidation of metals such as titanium and zirconium is characterized by both oxide formation and concurrent dissolution of gas into the metal (ref. 8).

Models applied to partition the total oxygen uptake during oxidation exposure into these two components have been described by several authors (refs. 9-12). Even though these models are substantially true in explaining the oxidation of the alloys of titanium as well, they do not provide an adequate basis to account for the role of the alloying elements in controlling the oxidation rate. Accordingly, in the present study, a theoretical analysis has been developed to integrate Wagner's theory (ref. 13) of oxidation into a model for titanium oxidation developed by Unnam et al. (ref. 12) so that the defect structure of the oxide lattice can be taken into account. This approach enables one to determine the effect of alloying elements as dopants in controlling the oxidation kinetics of alloys. The model has been applied to predict the oxidation behavior of Ti-14Al-21Nb alloy, and the results have been compared with experimental data.

Oxidation kinetics were measured in laboratory air using thermogravimetry and covered a temperature range from 649°C to 1093°C. The oxidized specimens were examined using X-ray diffraction (XRD), light and scanning electron microscopy (SEM), microprobe X-ray analysis, energy dispersive X-ray analysis (EDS), and Auger electron spectroscopy (AES) to characterize the oxidation products and microstructural changes in the alloy.

Theory

Figure 1 shows a schematic diagram of the oxidation process and emphasizes that, at equilibrium, the chemical potential of oxygen is continuous across a two-phase interface even though the concentration gradients can show a discontinuity. The formation of an oxide scale of finite thickness on the metal implies that the oxide growth rate is faster than the dissolution process. Therefore, the total oxidation rate is essentially governed by the transport characteristics of the oxide compound (refs. 13 and 14), so that

$$\frac{d}{dt}\left(\frac{m}{A}\right)_{total} = \frac{\overline{m}k_r}{z} \qquad \left(\overline{m} = \frac{M_O}{Z_2}\right) \quad (1)$$

where

$\frac{d}{dt}\left(\frac{m}{A}\right)_{total}$	flux of oxygen uptake, $g/cm^2/sec$
z	instantaneous oxide thickness, cm
k_r	rational rate constant defined by Wagner (ref. 14), eq/cm/sec (where eq in the unit denotes equivalents)
$\overline{m}$	equivalent weight of oxygen, g/eq
M_O	atomic weight of oxygen, g
Z_2	valency of oxygen ions in the oxide

Under steady-state conditions, k_r is a constant and is a fundamental property of the oxide compound. On the other hand, the thickness of the oxide formed on metals such as titanium and their alloys, which have a high solubility for oxygen, is governed by the partitioning of the oxygen toward the dissolution process. Thus, a complete description of the total oxygen uptake during the oxidation of such metals/alloys requires a knowledge of two parameters: the rational rate constant k_r and the instantaneous oxide thickness z.

Combining the defect structure properties of the oxide compound with its thermodynamic and electrochemical properties, and making certain simplifying assumptions, allowed Wagner (ref. 14) to derive the rational rate constant k_r as

$$k_r = \frac{C_{eq}}{RT} \int_{\mu_O''}^{\mu_O'} \left(\frac{Z_1}{|Z_2|} D_1 + D_2 \right) d\mu_O \qquad (2)$$

where

C_{eq}	equilibrium concentration of metal ions or oxygen ions, eq/cm^3
Z_1	valence of metal ions
Z_2	valence of oxygen ions
μ_O'	chemical potential of oxygen at oxide/gas interface
μ_O''	chemical potential of oxygen at oxide/metal interface (or outer-oxide/inner-oxide interface in the case of multiple oxides)
μ_O	chemical potential of oxygen at any arbitrary position in the oxide
D_1	self-diffusion coefficient of metal ions in the oxide, cm^2/sec
D_2	self-diffusion coefficient of oxygen ions in oxide, cm^2/sec
R	universal gas constant, cal/mol-K
T	absolute temperature, K

If one expresses the chemical potentials in terms of activities and notes that activities can be expressed in terms of the partial pressure of oxygen for a solid in equilibrium with a diatomic gas, the equation

$$\mu_O = \mu_O^o + RT \ln a_O \qquad (a_O = P_{O_2}^{1/2}) \qquad (3)$$

can be written where

μ_O^o	standard chemical potential of oxygen
a_O	activity of oxygen
P_{O_2}	partial pressure of oxygen in gas phase with which the solid is in equilibrium

Accordingly, k_r can be redefined as

$$k_r = \frac{C_{eq}}{2} \int_{P_{O_2}''}^{P_{O_2}'} \left(\frac{Z_1}{|Z_2|} D_1 + D_2 \right) d \ln P_{O_2} \qquad (4)$$

where

P_{O_2}'	partial pressure of oxygen at oxide/gas interface
P_{O_2}''	dissociation pressure of oxygen corresponding to oxide/metal (or outer-oxide/inner-oxide) equilibrium

The significance of this definition for the rate constant k_r is that it can be predicted from independently measured values of the self-diffusion coefficients of the metal ions and oxygen ions in the oxide compound and also from the thermodynamic properties of the oxide. Unfortunately, since migration of ions in ionic compounds occurs through defect sites in the lattice, and the defect concentrations are dependent on the nonmetal activity (ref. 15), the diffusion coefficients are a function of the oxygen pressure and such data are not readily available. However, for many oxides, tracer-diffusion-coefficient data after equilibration to a specific oxygen pressure (usually pure oxygen at 1 atm) are available and the defect structure data are also known; thus, from a knowledge of the defect equilibria and the dominant defect in the oxide, the oxygen pressure dependence of the diffusion coefficients of the ions can be established.

TiO$_2$ is known to be an n-type semiconductor (refs. 15 and 16), but disagreements exist on whether interstitial cations or oxygen vacancies are the predominant defects in the oxide. Based on studies of nonstoichiometry of TiO$_2$ as a function of temperature and oxygen partial pressure, Kofstad (ref. 16) concluded that the defect structure of TiO$_2$ is composed of both types of defects. He further determined that the oxygen vacancies are doubly ionized and the interstitial ions are composed of two kinds: Ti^{3+} and Ti^{4+}. However, marker experiments performed during the oxidation of titanium between 800°C and 1200°C (refs. 6 and 8) reveal that oxygen ions are the mobile species in TiO$_2$, implying that doubly ionized

oxygen ion vacancies are the predominant defect in the oxide and that the diffusivity of oxygen ions is larger than that of titanium ions (i.e., $D_2 \gg D_1$). From a mechanistic point of view, D_2 can be related to the concentration of doubly ionized oxygen ion as

$$D_2 = \left[V_{\ddot{O}}\right] \cdot D_V \qquad (5)$$

where

D_V diffusivity of oxygen ion vacancies in TiO_2

$\left[V_{\ddot{O}}\right]$ concentration of oxygen ion vacancies

The designation of the symbol $V_{\ddot{O}}$ for doubly ionized oxygen vacancies follows the notation developed by Kröger and Vink (ref. 17). In this notation, the symbol denotes the defect species, the subscript denotes the site, and the superscript designates the effective charge of the defect relative to the lattice. For dilute concentration of vacancies, it can be assumed that no defect interactions occur and that D_V is independent of the oxygen pressure. Thus, equation (4) can be further reduced to

$$k_r = \frac{C_{eq}}{2} D_V \int_{P_{O_2}''}^{P_{O_2}'} \left[V_{\ddot{O}}\right] d \ln P_{O_2} \qquad (6)$$

Thus, any oxygen pressure dependence of the oxidation kinetics of oxygen-deficient oxides is brought about by the oxygen-pressure-dependent concentration of oxygen ion vacancies in the lattice.

The formation of doubly ionized oxygen vacancies in the TiO_2 lattice can be described through the following equilibria (ref. 15):

$$\left.\begin{array}{l} O_O \rightleftharpoons V_O^x + \frac{1}{2}O_2 \\[6pt] V_O^x \rightleftharpoons V_{\dot{O}} + e' \\[6pt] V_{\dot{O}} \rightleftharpoons V_{\ddot{O}} + e' \end{array}\right\} \qquad (7)$$
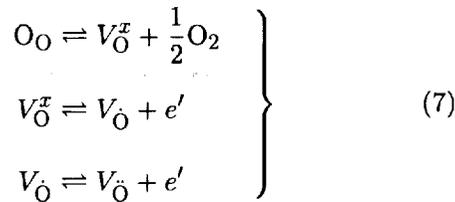
and by combining the above equations and using the laws of mass action:

$$\left.\begin{array}{l} O_O \rightleftharpoons V_{\ddot{O}} + \frac{1}{2}O_2 + 2e' \\[6pt] K = P_{O_2}^{1/2} \cdot \left[V_{\ddot{O}}\right] \cdot n^2 \end{array}\right\} \qquad (8)$$

where

O_O oxygen ion occupying a normal site in the oxide

V_O^x neutral oxygen ion vacancy in which both electrons are associated with the vacancy

$V_{\dot{O}}$ singly ionized oxygen ion vacancy in which only one of the electrons is associated with the vacancy

$V_{\ddot{O}}$ doubly ionized oxygen ion vacancy from which both electrons are freed

e' electron

n concentration of electrons

K equilibrium constant

The electrical neutrality requirements of the crystal dictate that the positive and negative charges be balanced, i.e., that $2\left[V_{\ddot{O}}\right] = n$. Thus, the concentration of the vacancies can be written as

$$\left[V_{\ddot{O}}\right] = \frac{K^{1/3}}{4^{1/3}} P_{O_2}^{-1/6} \qquad (9)$$

Since K is a constant at any given temperature, this relationship establishes the oxygen pressure dependence of the concentration of oxygen ion vacancies in a pure TiO_2 crystal.

In a doped crystal of TiO_2, the oxygen pressure dependence of the vacancies can be altered by the dopant ion, depending on its valency and concentration in the oxide. Thus, if Nb_2O_5, a higher-valent cation, dissolves in TiO_2, the process results in the annihilation of oxygen vacancies through the reaction

$$Nb_2O_5 + V_{\ddot{O}} \rightleftharpoons 2Nb_{\dot{T}i} + 5O_O \qquad (10)$$
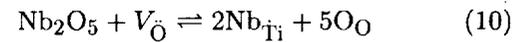
Here, $Nb_{\dot{T}i}$ is the Nb^{5+} ion occupying a normal Ti^{4+} site, which has a unit positive charge relative to the lattice. The electroneutrality condition for this case becomes

$$2\left[V_{\ddot{O}}\right] + \left[Nb_{\dot{T}i}\right] = n \qquad (11)$$

When $\left[Nb_{\dot{T}i}\right] \gg \left[V_{\ddot{O}}\right]$, $\left[Nb_{\dot{T}i}\right] \approx n$ and the concentration of vacancies is obtained from equation (8) after appropriate substitution. Thus,

$$\left[V_{\ddot{O}}\right] = \frac{K}{\left[Nb_{\dot{T}i}\right]^2} P_{O_2}^{-1/2} \qquad (12)$$

On the other hand, if $\left[V_{\ddot{O}}\right] \gg \left[Nb_{\dot{T}i}\right]$, i.e., if the native defect concentration is greater than the concentration of the dopant, then $2\left[V_{\ddot{O}}\right] \approx n$, from

3

equation (11), and the vacancy concentration is given by equation (9). Thus, in this case the dopant does not control the defect structure of the oxide.

In an analogous manner, it can be shown that the addition of a lower-valent cation to the TiO$_2$ lattice will result in the creation of oxygen ion vacancies. For example, if Al$_2$O$_3$ is dissolved into TiO$_2$, it will result in the generation of oxygen vacancies through the reaction

$$Al_2O_3 \rightleftharpoons 2Al'_{Ti} + 3O_O + V_{\ddot{O}} \qquad (13)$$
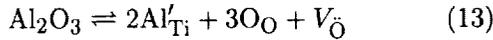
Here, Al$'_{Ti}$ is the Al^{3+} ion occupying a normal Ti^{4+} site that has a unit negative charge relative to the lattice. The electroneutrality requirement for this case can be written as

$$n + 2\left[Al'_{Ti}\right] = 2\left[V_{\ddot{O}}\right] \qquad (14)$$

Again, two possibilities arise: if the dopant concentration is too small, i.e., if $n \gg [Al'_{Ti}]$, then $n \approx 2\left[V_{\ddot{O}}\right]$ and the vacancy concentration is the same as that of a pure TiO$_2$ crystal as given by equation (9). However, if $\left[Al_{Ti}'\right] \gg n$, then

$$\left[V_{\ddot{O}}\right] = [Al'_{Ti}] \qquad (15)$$

Equations (9), (12), and (15) provide a basis to determine the equilibrium concentration of oxygen ion vacancies in undoped or doped TiO$_2$. In principle, if one knows the concentration of oxygen ion vacancies, the rate constant for oxidation can be predicted from equation (6). However, a major difficulty in evaluating the rate constant from equation (6) is that D_V (the diffusion coefficient for the vacancies in TiO$_2$) is not a measurable parameter. However, since independent measurements of tracer diffusion coefficient of oxygen in pure TiO$_2$ equilibrated to 1 atm oxygen are available in the literature, D_V can be extracted from such data using equations (5) and (9) as

$$D_V = \frac{4^{1/3}D_2^*}{fK^{1/3}} \qquad (16)$$

where

D_2^* tracer diffusion coefficient of oxygen in TiO$_2$

f correlation factor for diffusion

Making a simplifying assumption that D_V is not significantly affected by the small concentration of dopant ions in the TiO$_2$ lattice allows the rational

rate constant to be determined for each of the following three cases by appropriate substitutions into equation (6) and integration:

(1) For pure TiO$_2$,

$$k_r = \frac{3C_{eq}}{f}D_2^*\left[(P''_{O_2})^{-1/6} - (P'_{O_2})^{-1/6}\right] \qquad (17a)$$

(2) For TiO$_2$ doped with Nb^{5+},

$$k_r = 4^{1/3}\frac{C_{eq}D_2^*}{f}\frac{K^{2/3}}{\left[Nb_{Ti}^{\cdot}\right]^2}\left[(P''_{O_2})^{-1/2}\right.$$
$$\left. -(P'_{O_2})^{-1/2}\right] \qquad (17b)$$

(3) For TiO$_2$ doped with Al^{3+},

$$k_r = 4^{-1/6}\frac{C_{eq}D_2^*}{f}\frac{[Al'_{Ti}]}{K^{1/3}}\ln\left[\frac{P'_{O_2}}{P''_{O_2}}\right] \qquad (17c)$$

Since the dissociation pressure of titanium oxides is extremely low, i.e., $P'_{O_2} \gg P''_{O_2}$, the oxide growth rate becomes independent of the oxygen pressure in the environment.

Having established a relationship to compute the rational rate constant k_r in terms of the fundamental properties of the oxide compound, equations (17) in combination with equation (1) can be used to predict the oxidation rate of titanium and its alloys. However, solution of equation (1) still requires a knowledge of the instantaneous thickness of the oxide. With suitable conversion of units, the oxide thickness can be expressed in terms of the weight gain components:

$$z = \left(\frac{\overline{V}}{\overline{m}}\right)\left[\left(\frac{m}{A}\right)_{total} - \left(\frac{m}{A}\right)_{alloy}\right] \qquad (18)$$

where

$(m/A)_{total}$ total weight gain associated with oxidation process, g/cm^2

$(m/A)_{alloy}$ component of weight gain due to dissolution process, g/cm^2

$\overline{V}$ equivalent volume of oxide compound, cm^3/eq

Substitution of equation (18) into equation (1) yields the differential equation governing the oxidation rate

of metals/alloys that exhibit concurrent oxide forma-
tion and oxygen dissolution:

$$\frac{d}{dt}\left(\frac{m}{A}\right)_{\text{total}} = \frac{\overline{m}^2 k_r}{\overline{V}\left[\left(\frac{m}{A}\right)_{\text{total}} - \left(\frac{m}{A}\right)_{\text{alloy}}\right]} \quad (19)$$

The solution of equation (19) to determine the
time dependence of the oxidation rate in terms of
the known parameters requires some simplifications
to be made. First, assuming that diffusive processes
are rate controlling, the oxidation rate follows a
parabolic behavior:

$$\left.\begin{array}{l}\left(\dfrac{m}{A}\right)_{\text{total}} = k_p t^{1/2} \\[2mm] \dfrac{d}{dt}\left(\dfrac{m}{A}\right)_{\text{total}} = \dfrac{k_p}{2t^{1/2}}\end{array}\right\} \quad (20)$$

where

k_p weight-gain parabolic-rate constant,
$\quad$ g/cm^2/sec$^{1/2}$

t duration of oxidation exposure, sec

Second, as adequately described by Unnam et al. in
reference 12, an independent solution is available for
determining the oxygen dissolution in titanium and
its alloys in terms of the fundamental properties of
the metal/alloy; consequently,

$$\left(\frac{m}{A}\right)_{\text{alloy}} = k_d t^{1/2} \quad (21)$$

with

$$k_d = 2f_0(C_{sl} - C_0)\left(\frac{D_s}{\pi}\right)^{1/2}$$

where

k_d rate constant pertaining to oxy-
$\quad$ gen dissolution in metal/alloy,
$\quad$ g/cm^2/sec$^{1/2}$

C_{sl} concentration of oxygen in the alloy
$\quad$ at alloy/oxide interface, atomic
$\quad$ percent

C_0 oxygen concentration deep in the
$\quad$ alloy, atomic percent

f_0 conversion factor to express con-
$\quad$ centrations in grams per cubic
$\quad$ centimeter

D_s oxygen diffusivity in the alloy,
$\quad$ cm^2/sec

t duration of exposure, sec

Substitution of equations (20) and (21) into (19)
leads to the solution

$$\left(\frac{m}{A}\right)_{\text{total}} = \frac{k_d + \left(k_d^2 + \frac{8\overline{m}^2 k_r}{\overline{V}}\right)^{1/2}}{2}t^{1/2} \quad (22)$$

Thus,

$$k_p = \frac{k_d + \left(k_d^2 + \frac{8\overline{m}^2 k_r}{\overline{V}}\right)^{1/2}}{2} \quad (23)$$

The significance of the development of equa-
tion (22) is that the overall weight-gain parabolic-
rate constant k_p is directly related to fundamen-
tal constants that describe the transport proper-
ties in the metal/alloy and in the oxide compound.
Two limiting conditions can be observed from equa-
tion (23): in the first case, if $k_d \gg k_r$, then

$$k_p = k_d \quad (24a)$$

In this case the oxygen-uptake-rate constant is
solely governed by the dissolution process in the
metal/alloy. In the second case, if $k_r \gg k_d$, then

$$k_p = \left(\frac{2\overline{m}^2 k_r}{\overline{V}}\right)^{1/2} \quad (24b)$$

In this case the oxygen-uptake-rate constant is essen-
tially controlled by the transport through the oxide
compound.

How well the kinetic model described up to this
time adequately explains the oxidation behavior of
Ti-14Al-21Nb alloy can be corroborated by compar-
ing the experimental rate constant k_p determined
from the TGA data with that computed from equa-
tions (23) and (24).

Experimental Details

Specimens and Materials

The chemical analysis of the hot-rolled Ti-14Al-
21Nb ingot alloy is shown in table I. Thermogravi-
metric analysis (TGA) samples (approximately 1 cm
by 1.5 cm by 0.2 cm with a nominal surface area of
4 cm^2) were cut from the ingot alloy using a slow-
speed diamond saw. A 0.16-cm-diameter hole was
drilled at one end of the sample to facilitate hang-
ing from the microbalance during the oxidation ex-
posure. Prior to the test, the samples were ground to
a uniform surface finish by grinding with silicon car-
bide papers ranging from 240 grit (60 μm was the av-
erage grinding particle size) through 600 grit (15 μm

was the average grinding particle size). After grinding, the dimensions of the samples were measured to the nearest 0.001 cm. The samples were then thoroughly cleaned with soap solution, acetone, and ethyl alcohol, and then they were dried in air. The initial weights of the cleaned samples were recorded to the nearest 0.05 mg.

Oxidation Studies

Oxidation tests were conducted in laboratory air over the temperature range from 649°C to 1093°C in two types of TGA apparatus. For the temperature range from 649°C to 871°C, the tests were performed in an apparatus in which the weight of the sample was monitored with a Cahn R-100 microbalance. Although this apparatus had the sensitivity required for even small weight changes, it was not designed for use at temperatures above 900°C. Therefore, for the temperature range from 871°C to 1093°C, the tests were performed in a Netzsch simultaneous thermal analysis (STA) unit, which is a combination TGA/DTA (differential thermal analysis) apparatus. Correlation of the data obtained from the two apparatus units was confirmed through the overlapping data from both apparatus units at 871°C.

In conducting these tests, the following sequence of steps was followed: first, the sample was introduced into the TGA setup; second, the microbalance zeroed; and third, the furnace temperature raised from room temperature to the test temperature over a period of about 30 minutes. The change in the weight of the sample was monitored from the start of the furnace heat-up. The temperature of the sample was monitored through a separate thermocouple located about 0.1 cm below the sample.

At each temperature, duplicate or triplicate tests were performed to ensure reproducibility in the data. Most samples were oxidized for a period of about 25 hr at temperature, but in some cases the oxidation runs were continued for a period of about 120 hr to study the effects of long-term exposure. At the end of each test, the sample was cooled rapidly by cutting off the electrical power to the furnace. At the end of each test, the final weight of the sample was recorded to the nearest 0.05 mg.

Characterization Studies

After oxidation, selected samples were analyzed by XRD, electron microprobe analysis, EDS, and AES. The cross sections of a few samples were examined using conventional light microscopy and SEM. Cross-sectional metallographic samples were prepared by first wrapping them in aluminum foil, hot mounting them in a special edge-retaining resin,

and utilizing the usual polishing techniques. A few of the samples were etched with Kroll's reagent (2 percent HNO_3 + 1 percent HF + 97 percent H_2O) to study the effect of oxidation on the alloy microstructure. Oxide thicknesses were determined from photomicrographs of the cross sections.

Results and Discussion

Weight Gain Kinetics

Figure 2 shows a typical output of the TGA data plotted in parabolic coordinates, (with weight gain normalized to unit area of the sample as a function of the square root of time). The apparent weight loss and nonlinearity in the data early in the exposure period result from transient temperature and buoyancy effects. These effects vanish within 1 hr from the start of a test.

Because of these transient effects, the TGA data for the first hour were discarded and the time scale was adjusted by replacing the heat-up time with an equivalent time at oxidation temperature, computed using an estimated activation energy for the oxidation process. Further, the total weight gain determined from the initial and final weights of the sample was used to adjust the TGA data to the true weight gain. Figure 3(a) shows the final TGA data for the samples oxidized from 649°C to 871°C, and figure 3(b) shows the data for the temperature range from 871°C to 1093°C.

From figure 3 it can be surmised that the oxidation of this alloy follows parabolic kinetics, but it is characterized by two or more slopes separated from each other by distinct transitions. It appears that these transitions are marked by specific weight gain values. Also, the presence or absence of these transitions is dependent on the temperature and duration of exposure at temperature. For instance, the first transition at 0.25 mg/cm^2 is distinctly noted for the samples exposed at 760°C and 816°C, whereas both the first and second transitions (at 0.5 mg/cm^2) are pronounced only for the sample exposed at 871°C. None of these transitions is observable for the samples oxidized at 649°C and 704°C; it is evident from figure 3(a) that the oxidation duration at these temperatures was not long enough to approach the specific weight gain needed for these transitions. For the samples oxidized at higher temperatures (982°C and 1093°C), the weight gain rates were so high (fig. 3(b)) that these transitions could not be identified from the TGA data. It is safe to assume that these transitions must have occurred at the very early stage of oxidation at these temperatures, with the result that the kinetics of these samples were dominated by the third slope.

The measured rate constants, i.e., the slopes of the weight gain data from figure 3, as well as the other relevant details for each of the tests are listed in table II and plotted in figure 4. The results highlight the complexity in the oxidation behavior of this alloy and suggest the existence of several operating mechanisms depending on the temperature and duration of exposure. For example, the stage I rate constants show an activation energy of approximately 85 kcal/mol over the temperature range from 649°C to 760°C, but they approach a value of approximately 54 kcal/mol over the temperature range from 760°C to 871°C. On the other hand, the stage II and stage III kinetics show activation energies of 54 kcal/mol and 64 kcal/mol, respectively.

Characteristics of Oxide Layer

Samples exposed to temperatures up to 760°C retained the specular finish of the metal surface, but the color of the metal changed gradually from golden to black as the temperature of exposure was increased. On the other hand, the color of the scales changed from black to dark gray as the exposure temperature was increased from 816°C to 982°C. The samples oxidized at 1093°C spalled, perhaps during the cooling cycle after oxidation since the TGA data did not reveal any abnormalities usually associated with spalling. The outer surface of the spalled oxide appeared gray in color, but the inner surface of the spalled oxide and the residual oxide on the metal appeared black in color.

XRD analysis of the scales from a few samples representing the three kinetic stages of figures 3 and 4 is summarized in table III. TiO_2, TiN, and Al_2O_3 were the principal phases observed in the oxide. The relative proportions of these compounds in the scale were calculated from the measured X-ray peak heights after applying the appropriate linear reflectivity coefficients. The latter parameter was calculated from the structure factors for each material and reflection. In performing these calculations, it was assumed that the oxides were thin relative to the working depth; and because the width of the entrance slit of the diffractometer was proportional to $\sin \theta$, it was not necessary to correct for the oxide thickness. It was further assumed that the oxide crystals were randomly oriented. The calculations yielded compositions in terms of volume percent, and the resulting numbers were rounded off to the nearest 5 percent, the confidence limit of the estimation. It is significant to note that although the predominant oxidation product in all the cases was TiO_2, the samples from stage I showed very little of reaction products, stage II showed some TiN, and stage III showed Al_2O_3. It is also interesting to note that the

sample oxidized at 871°C (which displayed all three stages of oxidation) showed both TiN and Al_2O_3 to be present in the product. The results also seem to indicate that the proportion of TiN in the scale decreases and that of Al_2O_3 increases with an increase in the temperature of oxidation.

Oxide thickness measurements after oxidation were obtained from cross-sectional metallography. However, the range of temperatures for which these data could be obtained was limited because the samples that oxidized at lower temperatures (such as 649°C, 704°C, and 760°C (short term)) showed no discernible reaction products in the cross-sectional metallographs. Also, since the samples exposed at 1093°C spalled, the oxide thickness data could not be obtained for this temperature of exposure as well. The limited data from the remaining exposure conditions are presented in table IV. Using the oxide thickness measurements and the total weight gain values obtained from weight measurements before and after exposure allowed the isolation of the contributions to oxide formation and metal dissolution. These results are also presented in table IV.

Both SEM and EDS were used to further characterize the morphology and composition of the oxides. Again, these studies had to be restricted to samples oxidized at 871°C and above since the samples oxidized at lower temperatures (649°C to 816°C) showed very little reaction products, and the cross section of these samples could not be resolved in the SEM. Figure 5 presents the secondary electron image of the cross section, and shows the EDS maps of Ti, Al, Nb, and O for a sample oxidized at 982°C for 24 hr. The oxide is characterized by layered porosity and fingers of particles close to the outer edge. Consistent with the XRD data, these studies also indicate that the scale is predominantly composed of TiO_2. The Al and Nb maps indicate that although the oxide is free of Al in the bulk, it has incorporated a substantial amount of Nb; the concentration of this element is seen to decrease from the inner edge to the outer edge. The finger regions show an enhancement of the Al signal intensity and a corresponding loss of the Ti intensity; a slight enhancement of the O intensity at these regions suggests these particles to be Al_2O_3. Since the XRD data did not detect any niobium oxides in the scale, Nb must be present in the TiO_2 as a dopant.

A similar conclusion can be drawn from the sample exposed at 1093°C for 24 hr and which had spalled. Figure 6 shows the appearance and the X-ray maps of Al and Ti of the outer side of the spalled oxide; an Nb map was not taken because of very low intensity. It is particularly significant to note that Al is distributed discretely along the

oxide surface, and also to note that in those regions where Al is present, Ti is absent. Figure 7 shows the morphology and X-ray maps of Ti and Nb of the underside of the spalled oxide. The EDS did not detect significant Al on the underside of the spalled oxide. The predominant features of the underside are a small grain size of the oxide and a fairly uniform distribution of Ti and Nb. Table V shows the results of the microprobe analysis of the spalled oxide. Principally, the analysis indicates the oxide to be predominantly TiO_2; Nb is seen on the inner surface and Al on the outer surface. Also, the data show a reasonable match between the analysis of the inner surface of the oxide and the residual oxide on the metal, indicating that spalling was not along any chemical interface. Calculations show the composition at the inner surface of the spalled oxide to be 90 percent TiO_2 and 10 percent Nb_2O_5, which is the maximum solubility for Nb_2O_5 in TiO_2 (refs. 7, 18, and 19).

The appearance of layered porosity in the sample exposed to 982°C (fig. 5) and the occurrence of spallation of the oxide on samples exposed to 1093°C indicate that the layered porosity may be the major cause for spallation.

In order to characterize the oxidation products formed on the alloy surface after low-temperature exposures (649°C to 760°C (short term)), a few of those samples were examined by AES. A typical spectrum is shown in figure 8. A notable feature of the spectrum is the existence of a chemical shift of the low-energy aluminum lines, indicating the presence of Al_2O_3. The presence of titanium lines in the spectrum indicates the simultaneous existence of TiO_2 with Al_2O_3. However, reliable quantitative data on the distribution of these phases could not be obtained from the AES analysis.

It can be concluded from the characterization studies that TiO_2 is the main component of the scale and that a continuous protective layer of Al_2O_3 does not form on these alloys at all temperatures and exposure durations reported in this study. It has been suggested by Zelenkov and Osokin (ref. 1) that this alloy attempts to form a protective layer of Al_2O_3 at early stages of oxidation, but the depletion of Al in the alloy leads to the eventual breakdown of this layer and the subsequent formation of TiO_2. In support of this argument, Perkins et al. (ref. 5) have shown that the diffusivity of Al in the alloy is not rapid enough to compensate for the depletion of the element through oxide formation.

Characteristics of the Metal

Figure 9 shows the microstructure of the alloy in the as-received condition (no oxidation) and after ex-posure to a few selected oxidation conditions. The as-received alloy appears to consist of two phases of almost equal proportion. The composition of these two phases as determined by EDS analysis is presented in table VI; for comparison, the nominal analysis of the alloy is also presented. There is a partitioning of the elements, particularly Nb, between the two phases. From the Ti_3Al-Nb phase diagram quoted by Strychor et al. (ref. 20), hexagonal α_2 and body-centered cubic β are the expected phases in the alloy at all temperatures covered in this study. On the other hand, XRD data of the base alloy indicated the predominant structure to be hexagonal although some peak splitting was observed in all the peaks except in the (001) type. This result suggests that both phases are the same type but differ in composition. Al in Ti produces contraction of the lattice principally along the "a" axis, whereas Nb has very little effect in the Ti lattice; therefore, segregation of Nb would not be readily apparent from the diffraction data.

It is evident from figure 9 that the heat treatment associated with the oxidation process has significantly changed the microstructure of the alloy. In the alloy bulk, grain refinement and grain growth can be noted. In the vicinity of the oxide layer, as clearly seen for the sample oxidized at 982°C, there is a formation of a single-phase case and a skirted region very close to the metal/oxide interface. An EDS analysis of the skirted region showed an enhancement in the Al and Nb intensities and a corresponding decrease in the Ti intensity, with the composition of this layer approaching that of TiAl. On the other hand, the presence of only a single phase case indicates the stabilizing effect of oxygen on one of the two phases reported earlier.

Figure 10 summarizes a portion of the the XRD data corresponding to a 2θ range of approximately 37° to 40°; this range was selected to observe the effect of oxidation exposure on the (002) reflection of the alloy before and after oxidation exposure. Compositional broadening of the (002) line can be observed for the sample oxidized at 649°C (fig. 10(b)). For the samples oxidized at 760°C, only line shifts could be noted (fig. 10(c)). The existence of a line shift rather than line broadening for this exposure condition suggests that the metal is saturated with oxygen within the X-ray penetration depth of the alloy (approximately 9 μm). For the sample exposed to a high temperature (982°C), the oxide thickness was large enough that only weak intensities of the base-alloy reflections could be obtained (fig. 10(d)). Also, the (002) peak was overlapped by a series of peaks corresponding to a TiAl phase. From the compositionally broadened peak for the sample exposed

to 649°C (fig. 10(b)) and using the analytical technique developed by Wiedemann and Unnam (ref. 21), a very precise composition-depth profile was constructed as shown in figure 11. From this analysis, the maximum solubility of oxygen for this exposure was determined as 12.5 atomic percent. These results indicate that oxygen dissolution into the alloy is a significant process during oxidation exposures. Oxygen in titanium alloys has been shown to lower ductility, and this problem is likely to exist with the Ti-14Al-21Nb alloy also.

Suggested Mechanisms

The existence of at least three slopes in the oxidation kinetics of Ti-14Al-21Nb alloy with corresponding changes in activation energies (figs. 3 and 4) reflects the complexity of the oxidation behavior of the alloy. Before attempting to identify the causes for this behavior, a comparison of the measured rate constant with the theoretical predictions can be made to gain additional information. Figure 12 compares the predicted and measured rate constants k_p for Ti-14Al-21Nb alloy and commercial purity titanium (Ti-A55); the experimental data have been reproduced from figure 4 and the predicted values have been calculated according to equation (23). Since TiO$_2$ was the predominant oxide in the scale formed on Ti-14Al-21Nb and the oxide had a relatively low Al content but a substantial Nb content, k_r was calculated according to equation (17b) for the alloy and according to equation (17a) for commercial purity titanium. The parameters required for the computation of k_r and k_d and the sources for the data (refs. 12, 15, 18, 22–26) are listed in table VII. In spite of the multiple sources for the data for the theoretical estimate (table VII), the agreement between the predicted and measured values is reasonable, implying the validity of using the defect-structure-based model for predicting the oxidation of Ti-14Al-21Nb alloy.

The deviation of k_p from the predicted values associated with variations in the activation energies (figs. 4 and 12) indicates the dominance of different operating mechanisms as a function of temperature. Indeed, this behavior was expected because examination of equation (23) shows that the rate constant k_p is in fact comprised of two temperature-dependent terms, k_r and k_d, and the dominance of one term or the other on the oxidation kinetics at a given temperature can give rise to the observed effect. However, the existence of at least three slopes during the isothermal oxidation of the alloy (fig. 3) suggests that the duration of exposure also causes changes in the operating mechanism. The existence of such transitions has been noted by several past investigators

(refs. 8, 9, 12, and 27). Kofstad et al. (ref. 8) and Wallwork and Jenkins (ref. 9) have suggested that the first-stage kinetics during the oxidation of titanium is predominantly controlled by the process of oxygen dissolution into the metal; the transition at the end of this stage is attributed to the onset of the oxide-formation process. The variations in the kinetics during the second and subsequent stages of oxidation have been attributed to cracking and healing processes in the oxide. An understanding of whether the observed transitions in the Ti-14Al-21Nb alloy are associated with changes in the metal-dissolution kinetics or oxide-formation kinetics will help in characterizing the oxidation behavior of this alloy.

In order to determine if the dissolution process had the major contribution to the observed kinetics, the oxygen diffusivity in the alloy was back-calculated from the oxidation data through equation (22) using the data from tables III and IV and taking $C_{sl} = 12.5$ atomic percent (figs. 10 and 11). Using the XRD data of the alloy to compute the density of the alloy-O solid solution allowed the conversion factor in equation (22) to be computed as $f_o = 0.0172$ g/cm^2/atomic percent-cm. Figure 13 shows the Arrhenius plot of the data; the 649°C data point was determined from the composition-depth profile in figure 11. Also shown in figure 13 is the plot of the oxygen diffusivity data from Wiedemann et al. (ref. 25). It is clear that the diffusivity values computed from oxidation kinetics data are up to an order of magnitude lower than that measured by Wiedemann et al. (ref. 25). On closer scrutiny of the data, it appears that the diffusivity data in figure 13 may be composed of two slopes as indicated by the dashed line.

The similarity in the trends between the first-stage kinetics (fig. 4) and the oxygen diffusivity in the alloy (the dashed curve in fig. 13), and the minimal oxide formation as evidenced by metallographic data, suggests that this stage of the oxidation process may be dominated by the oxygen dissolution kinetics. Taking cognizance of the variations in the alloy microstructure with exposure conditions (fig. 9), it seems probable that the variation in the activation energy during the first stage is due to the morphological effects. Thus, the samples exposed from 649°C to approximately 760°C may have alloy oxygen transport through a two-phase field, each having different diffusivities and solubilities. On the other hand, the dominance of one of these phases at higher temperatures (approximatly 760°C to 982°C) may be the cause for the drop in the activation energy. Eventually, the alloy surface forms a single phase case and this event possibly corresponds to a critical oxygen

9

content—the first transition may be a mark of this event.

The kinetics of the second and subsequent stages of oxidation of this alloy are possibly controlled by an oxide formation rate characterized by the rational rate constant k_r. Although XRD analysis shows small amounts of Al_2O_3 and TiN to be present in the scale, TiO_2 is the predominant oxide that is formed on the alloy surface for all the exposure conditions reported in this study. Hence, the kinetics during these stages are dominated by the transport properties of the TiO_2 layer. However, the TiO_2 compound is doped with Nb ions with the result that the oxygen transport through the oxide is limited by the reduction in concentration of oxygen ion vacancies caused by doping. At higher thicknesses of the oxide, layered porosity begins to occur because of alternating cracking and healing processes—the second transition may have been caused by this cracking.

Further oxidation studies on this alloy after suitable heat treatment to stabilize the microstructure are necessary to discern the microstructural effects.

Conclusions

The static oxidation kinetics of Ti-14Al-21Nb ingot alloy were studied in air over a temperature range from 649°C to 1093°C in a thermogravimetric apparatus. From this study the following conclusions are presented:

1. Ti-14Al-21Nb alloy has an oxidation resistance that is superior to that of commercial purity titanium or to other titanium alloys. However, the oxidation kinetics are complex; two distinct transitions separating three stages of differing activation energies are marked by specific weight gain values.

2. The oxide phase is predominantly composed of TiO_2, but small amounts of Al_2O_3 and TiN are also present. The TiO_2 has a substantial amount of Nb ions dissolved in it. Calculations show that Nb ions in TiO_2 reduce the concentration of oxygen ion vacancies, thereby reducing the diffusivity of oxygen through it. A reasonable agreement between the measured and calculated rate constants for oxidation supports this view.

3. High oxidation temperatures and long-term exposures at these temperatures result in layered porosity in the oxide—the onset of porosity is displayed by a change in the oxidation kinetics. It appears that healing of the outer layers results in continuously decreasing rate constants for samples exposed to very high temperatures ($\geq 982°C$). Also, the layered porosity may be responsible for spalling of the oxide.

4. The alloy has a substantial solubility for oxygen (≈ 12.5 atomic percent). In the absence of a prior high-temperature heat treatment after processing, oxidation exposures lead to changes in the microstructure of the alloy. Diffusivity of oxygen into the metal seems to be dependent on the alloy microstructure.

5. The alloy region close to the interface is enriched in Al and Nb; the role of this layer on oxidation kinetics needs further investigation.

References

1. Zelenkov, I. A.; and Osokin, E. N.: Oxidation Resistance of the Compound Ti 3Al and Its Alloys at Temperatures of 700 and 800 C. *Poroshkovaia Metallurgiia*, vol. 14, no. 10, Oct. 1975, pp. 72–75.

2. Zelenkov, I. A.; and Martynchuk, E. N.: Heat Resistance of Alloys of the Compound TiAl With Niobium at 800 and 1000 C. *Metallofizika*, no. 42, 1972, pp. 63–66.

3. Chaze, A. M.; and Coddet, C.: Influence of Alloying Elements on the Dissolution of Oxygen in the Metallic Phase During the Oxidation of Titanium Alloys. *J. Mat. Sci.*, vol. 22, Apr. 1987, pp. 1206–1214.

4. Streiff, R.; and Poize, S.: Oxidation of Aluminide Coatings on Unalloyed Titanium. *High Temperature Corrosion, Proceedings of Int. Conf., Nat. Assoc. Corrosion Engineers* (R. A. Rapp, ed.), 1983, pp. 591–597.

5. Perkins, R. A.; Chiang, K. T.; and Meier, G. H.: Formation of Alumina on Ti-Al Alloys. *Scr. Metall.*, vol. 21, no. 11, Nov. 1987, pp. 1505–1510.

6. Hauffe, Karl: *Oxidation of Metals*. Plenum Press, 1965, pp. 217–225.

7. Chen, Y. S.; and Rosa, C. J.: High-Temperature Oxidation of Ti-4.32 wt.% Nb Alloy. *Oxid. Met.*, vol. 14, no. 2, Apr. 1980, pp. 147–165.

8. Kofstad, P.; Anderson, P. B.; and Krudtaa, O. J.: Oxidation of Titanium in the Temperature Range 800–1200°C. *J. Less-Common Met.*, vol. 3, no. 2, Apr. 1961, pp. 89–97.

9. Wallwork, G. R.; and Jenkins, A. E.: Oxidation of Titanium, Zirconium, and Hafnium. *J. Electrochem. Soc.*, vol. 106, no. 1, Jan. 1959, pp. 10–14.

10. Wallwork, G. R.; Smeltzer, W. W.; and Rosa, C. J.: The Parabolic Oxidation Kinetics of Alpha-Zirconium at 850°C. *Acta Metall.*, vol. 12, no. 4, Apr. 1964, pp. 409–415.

11. Pemsler, J. P.: Studies on the Oxygen Gradients in Corroding Zirconium Alloys. *Jour. Nuclear Materials*, vol. 7, no. 1, 1962, pp. 16–25.

12. Unnam, J.; Shenoy, R. N.; and Clark, R. K.: Oxidation of Commercial Purity Titanium. *Oxid. Met.*, vol. 26, no. 3/4, Oct. 1986, pp. 231–252.

13. Wagner, Carl: Theory of the Tarnishing Process. *Z. Physik. Chem.*, vol. B, no. 21, 1933, pp. 25–41.

14. Wagner, Carl: Diffusion and High Temperature Oxidation of Metals. *Atom Movements, American Soc. for Metals*, c.1951, pp. 153–173.

15. Kofstad, Per: *Nonstoichiometry, Diffusion, and Electrical Conductivity in Binary Metal Oxides.* John Wiley & Sons, Inc., c.1972, pp. 15–46.

16. Kofstad, P.: *High-Temperature Oxidation of Metals.* John Wiley & Sons, Inc., 1966, p. 169.

17. Kröger, F. A.; and Vink, H. J.: Relations Between the Concentrations of Imperfections in Crystalline Solids. *Solid State Physics—Advances in Research and Applications, Volume 3*, Frederick Seitz and David Turnbull, eds., Academic Press, Inc., 1956, pp. 307–435.

18. Goldschmidt, H. J.: An X-Ray Investigation of Systems Between Niobium Pentoxide and Certain Additional Oxides. *Metallurgia*, vol. 62, no. 373, Nov. 1960, pp. 211–218.

19. Roth, R. S.; and Coughanour, L. W.: Phase Equilibrium Relations in the Systems Titania-Niobia and Zirconia-Niobia. *J. Res. National Bureau Stand.*, vol. 55, no. 4, Oct. 1955, pp. 209–213.

20. Strychor, R.; Williams, J. C.; and Soffa, W. A.: Phase Transformations and Modulated Microstructures in Ti-Al-Nb Alloys. *Metall. Trans.*, vol. 19A, no. 2, Feb. 1988, pp. 225–234.

21. Wiedemann, K. E.; and Unnam, J.: A Method of Rapidly Obtaining Concentration-Depth Profiles From X-Ray Diffraction. *J. Appl. Phys.*, vol. 58, no. 3, Aug. 1, 1985, pp. 1095–1101.

22. Shewmon, Paul G.: *Diffusion in Solids*, McGraw-Hill Book Co., Inc., 1963, p. 102.

23. Liu, Z.; and Welsch, G.: Communication: Literature Survey on Diffusivities of Oxygen, Aluminum, and Vanadium in Alpha Titanium, Beta Titanium, and in Rutile. *Metall. Trans*, vol. 19A, no. 4, pp. 1121–1125.

24. Kubaschewski, O.; and Alcock, C. B.: *Metallurgical Thermochemistry, Volume 24*, Fifth ed. Pergamon Press Ltd. (England), c.1979, p. 383.

25. Wiedemann, K. E.; Clark, R. K.; and Sankaran S. N.: *Emittance, Catalysis, and Dynamic Oxidation of Ti-14Al-21Nb.* NASA TP-2955, 1989.

26. Wiedemann, K. E.; and Unnam, J.: *An X-Ray Diffraction Study of Titanium Oxidation.* NASA CR-176263, 1984.

27. Shenoy, R. N.; Unnam, J.; and Clark, R. K.: Oxidation and Embrittlement of Ti-6Al-2Sn-4Zr-2Mo Alloy. *Oxid. Met.*, vol. 26, no. 1/2, Aug. 1986, pp. 105–124.

Table I. Chemical Analysis of Ti-14Al-21Nb Alloy

Element	Composition, percent weight	
	Nominal	Actual
Al	14	14.1
Nb	21	21.30
Mo		<.01
Fe		.09
V		<.01
C		.02
O		.13
N		.015
H		.0065
Zr		<.01
Ti	Balance	Balance

Table II. Thermogravimetric Analysis Results

Sample	Exposure conditions		Total weight gain, mg/cm^2	Weight gain rate,[a] μg/cm^2-$\sqrt{hr}$, for stage—		
	Temperature,°C	Time, hr		I	II	III
TA-5	649	102	0.087	2.53		
TA-7	649	112	.072	3.24		
TA-9	649	112	.062	3.62		
TA-1	704	24	.084	11.63		
TA-2	704	24	.092	11.58		
TA-3	704	25	.080	9.64		
TA-4	760	25	.250	45.6	40.1	
TA-6	760	24	.210	37.5	29.0	
TA-8	760	24	.210	41.2		
TA-18	760	116	.370	33.0	30.8	
TA-21	760	117	.390	35.0	30.7	
TA-10	816	24	.410	89.6	61.1	
TA-11	816	24	.380	84.5	62.6	
TA-12	816	24	.380	84.8	59.9	
TA-16	871	26	.740	135.5	103.5	138.6
TA-17	871	24	.730	126.6	114.0	142.9
TA-14	982	24	2.820			483.4
TA-15	1093	24	Spalled			1367.2
TA-19	1093	20	Spalled			1442.2

[a]The columns refer to the corresponding stages in figure 3.

Table III. Oxide Composition From X-Ray Diffraction Data

Exposure conditions			Estimated composition, percent volume		
Temperature, °C	Time, hr	Stage	TiO_2	Al_2O_3	TiN
760	25	I	70		30
760	117	II	75		25
816	24	II	75		25
871	26	III	80	10	10
982	24	III	75	25	

Table IV. Oxide Thickness and Partitioning of Oxygen

Sample	Exposure conditions		Oxide thickness,[a] μm	Weight gain, mg/cm^2	
	Temperature, °C	Time, hr		Oxide	Metal
TA-21	760	117	1.65	0.28	0.11
TA-10	816	24	1.45	.25	.16
TA-16	871	26	2.95	.50	.24
TA-14	982	24	13.65	2.32	.49

[a]Average of five measurements.

Table V. EDS Analysis of Spalled Oxide

Element	Composition, percent weight[a]		
	Outer surface	Inner surface	Residual oxide
Ti	50 (26)	40 (24)	40 (24)
Nb	0 (0)	20 (6)	22 (7)
O	44 (69)	40 (70)	37 (68)
Al	6 (5)	0 (0)	1 (1)

[a]Atomic percent is given in parentheses.

Table VI. Distribution of Elements Among Phases in Ti-14Al-21Nb Alloy

Element	Composition, percent weight[a]		
	Nominal	Dark phase	Light phase
Ti	65 (66)	64 (65)	69 (66)
Nb	21 (11)	23 (12)	16 (8)
Al	14 (25)	13 (23)	15 (26)

[a]Atomic percent is given in parentheses.

Table VII. Data for Theoretical Estimation of Rate Constant

Parameter	Value	Reference	Remarks
C_{eq}	0.21 eq/cm^3		
f	0.78	22	
D_2^*	$2.0 \times 10^{-3} \exp(-60\,000/RT)$	23	
	$1.7 \times 10^{-2} \exp(-66\,000/RT)$	23	
P_{O_2}''	$1.1 \times 10^{10} \exp(-146\,000/RT)$ (for undoped TiO$_2$)	24	P_{O_2}'' calculated for Ti$_3$O$_5$/TiO$_2$ equilibrium since Ti$_3$O$_5$ is next lowest stable phase
	$3.7 \times 10^{9} \exp(-156\,000/RT)$ (for TiO$_2$ doped with Nb)	24	P_{O_2}'' calculated for Ti$_3$O$_5$/TiO$_2$ equilibrium since Ti$_3$O$_5$ is unstable in presence of Nb
K	$4.0 \times 10^{2} \exp(-105\,000/RT)$	15	
$[\text{Nb}_{\text{Ti}}]$	0.2	18	Assumes maximum solubility
C_{sl}	25 atomic percent (pure titanium)	26	
	12.5 atomic percent (Ti-14Al-21Nb)	25	
D_s	2.7 $\exp(-51\,400/RT)$ (pure titanium)	26	
	0.0234 $\exp(-45\,090/RT)$ (Ti-14Al-21Nb)	25	
f_0	0.0178 (pure titanium)	12	
	0.0172 (Ti-14Al-21Nb)		Calculated from X-ray data
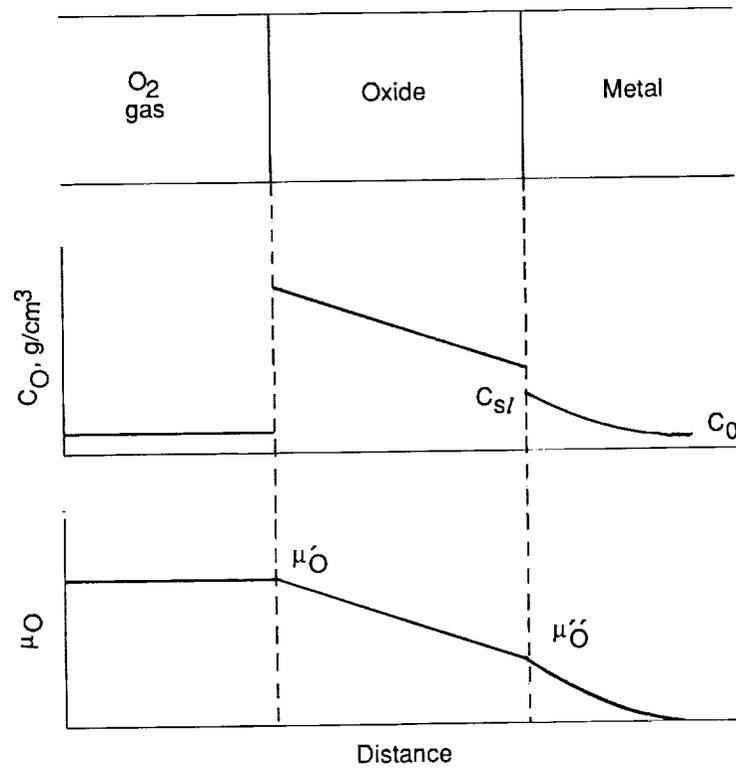
Figure 1. Schematic representation of oxidation process where oxygen distribution is presented in terms of concentration and chemical potential.
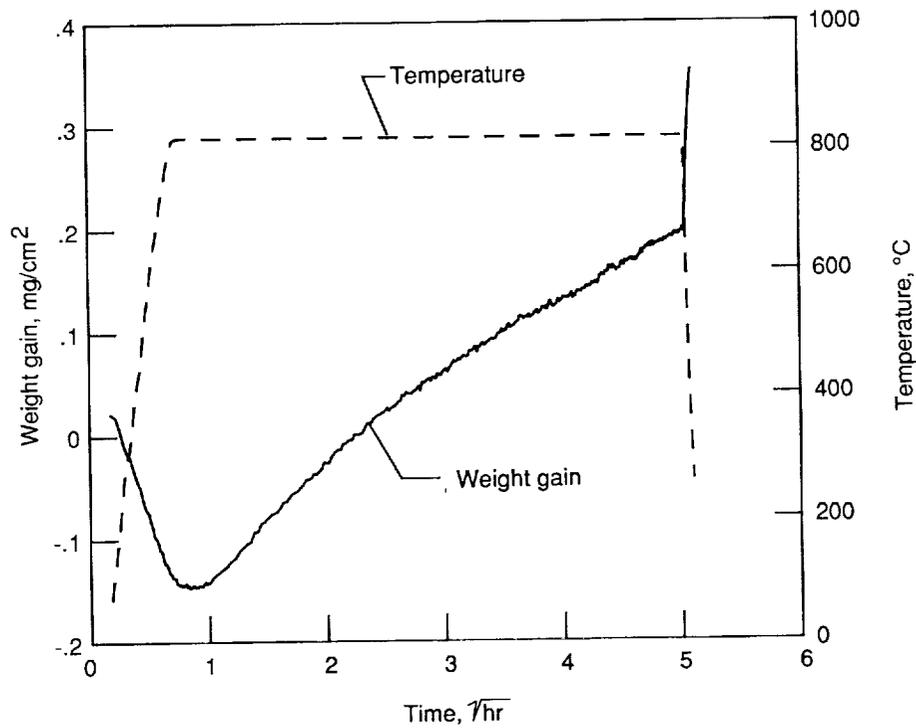
Figure 2. Typical output of TGA data for Ti-14Al-21Nb alloy.
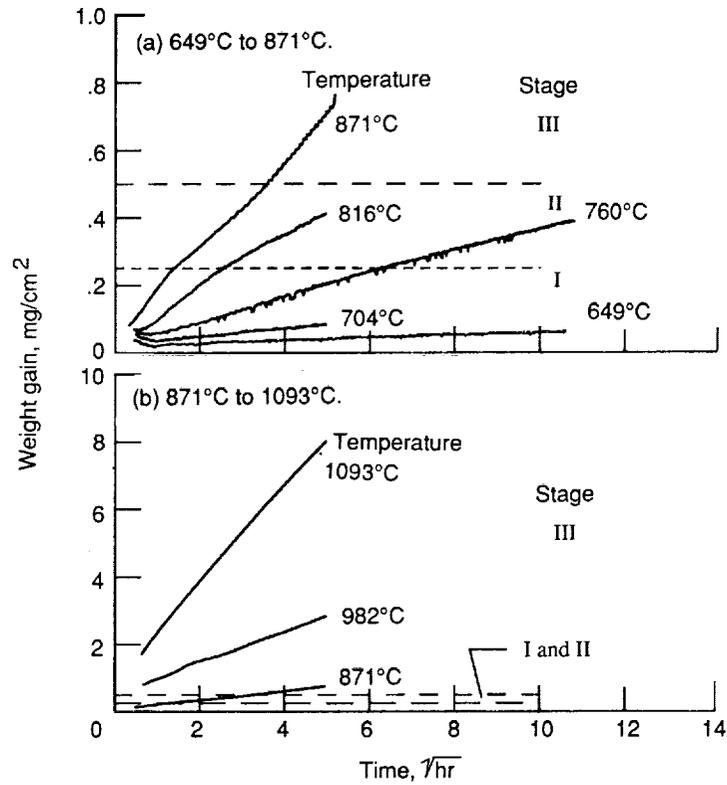
Figure 3. TGA results of Ti-14Al-21Nb alloy presented in parabolic coordinates. The two plots differ in scale.
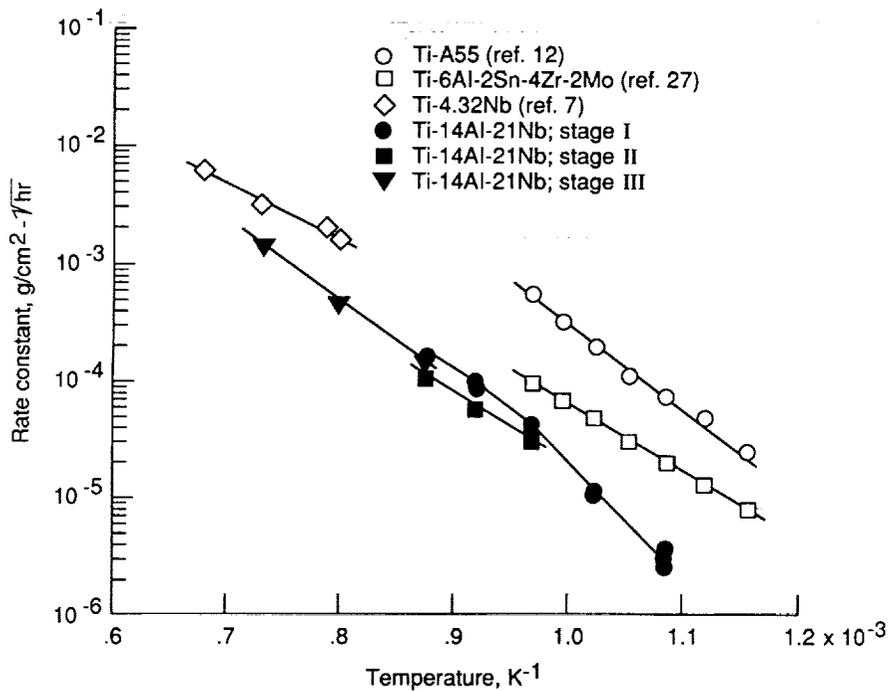

Figure 4. Arrhenius plot of oxidation rate constants for Ti-14Al-21Nb and other titanium alloys.
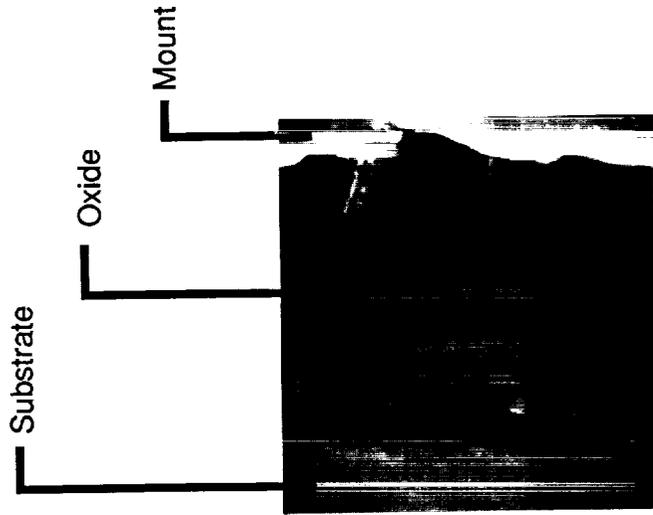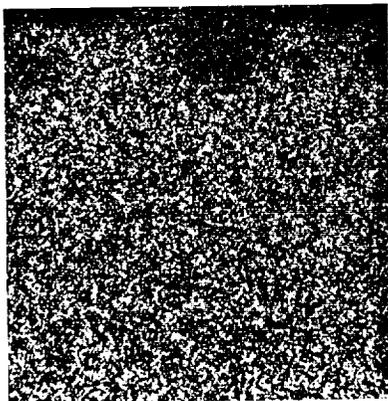
Figure 5. Secondary electron image of cross section and corresponding elemental maps of Ti-14Al-21Nb sample exposed at 982°C for 24 hours.

Micrograph

20 μm

Titanium map

Aluminum map
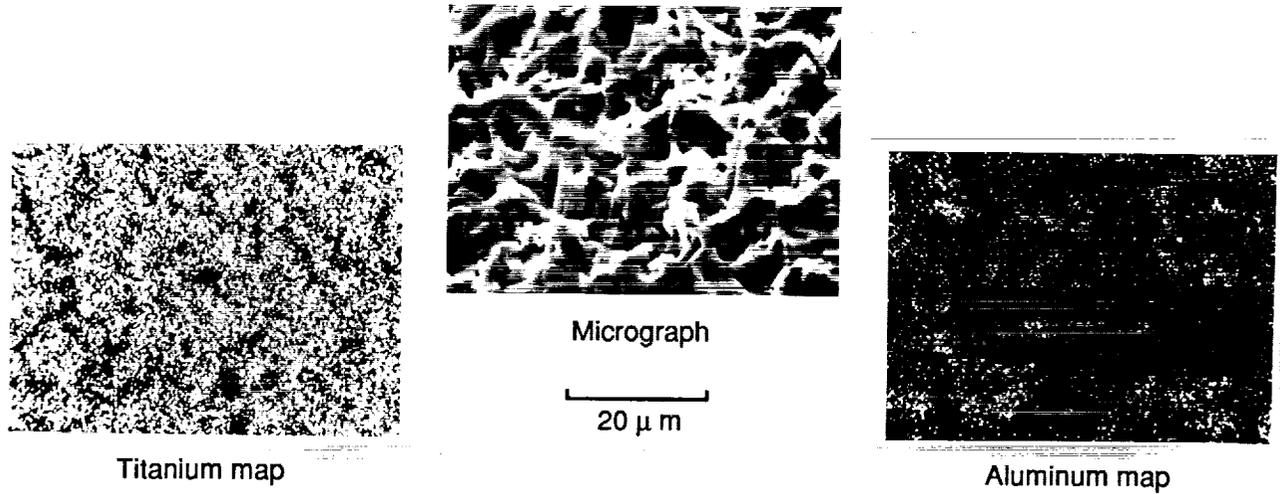
Figure 6. Secondary electron image and elemental maps of outer surface of spalled oxide of Ti-14Al-21Nb sample exposed at 1093°C for 24 hours.

Micrograph

Titanium map

Niobium map

10 μm
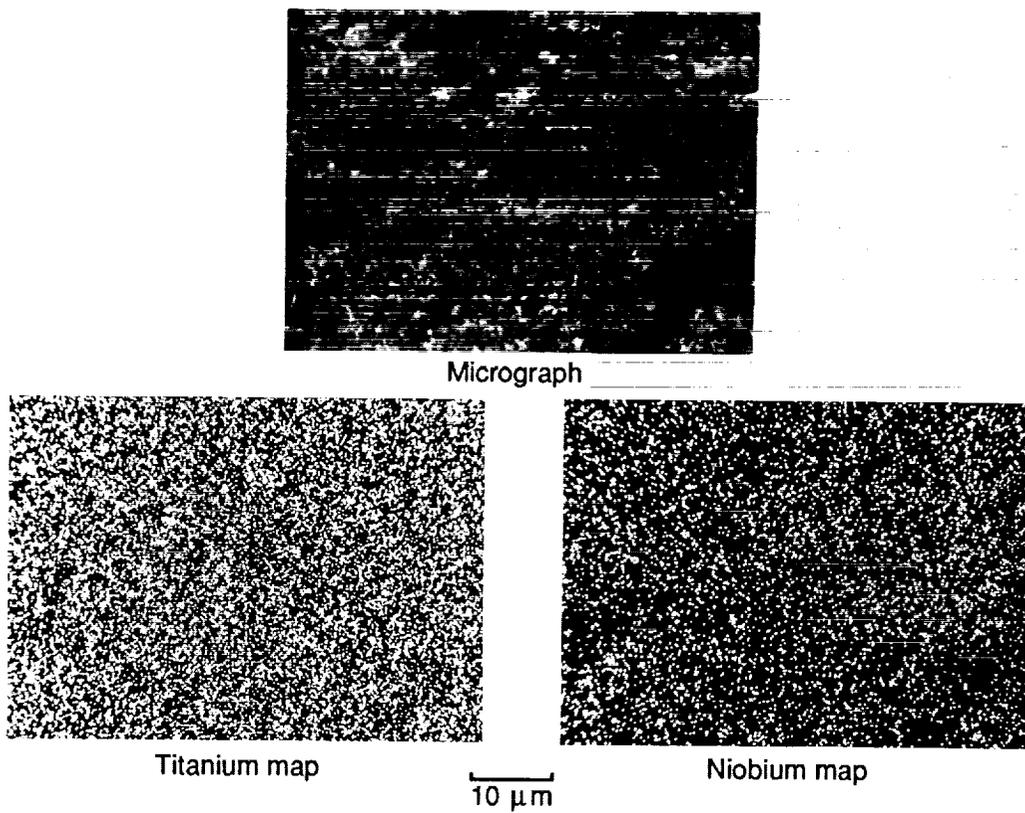
Figure 7. Secondary electron image and elemental maps of underside of spalled oxide of Ti-14Al-21Nb sample exposed at 1093°C for 24 hours.

18
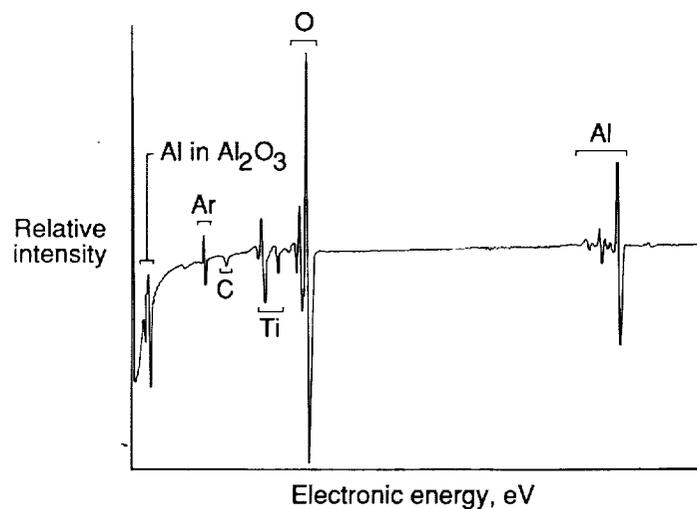
Figure 8. Typical AES of outer surface of Ti-14Al-21Nb sample during stage I kinetics.

No oxidation

816°C

50μm

704°C

982°C
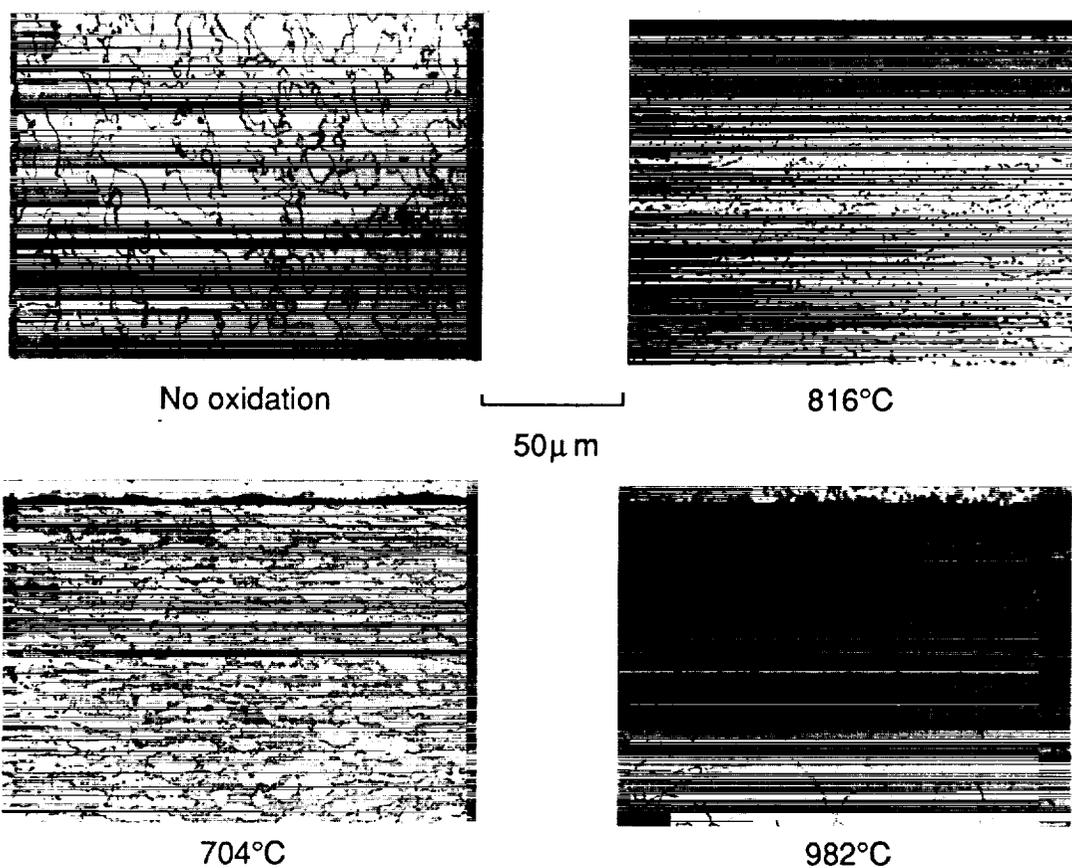
Figure 9. Cross-sectional micrographs of Ti-14Al-21Nb alloy after various oxidation exposures.
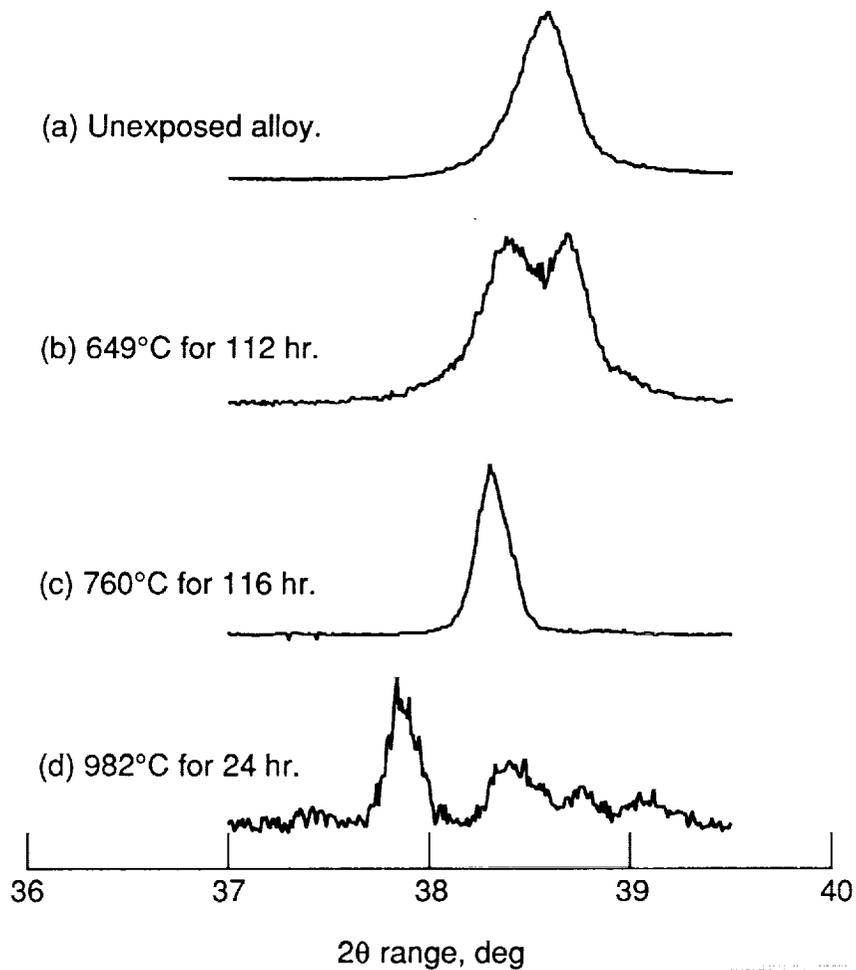
Figure 10. XRD data in 2θ range from approximately $37°$ to $40°$ for Ti-14Al-21Nb alloy after various oxidation exposures. Compositional broadening in part (b) and peak shift in part (c) are due to oxygen uptake. The new peaks seen in part (d) are from TiAl phase.
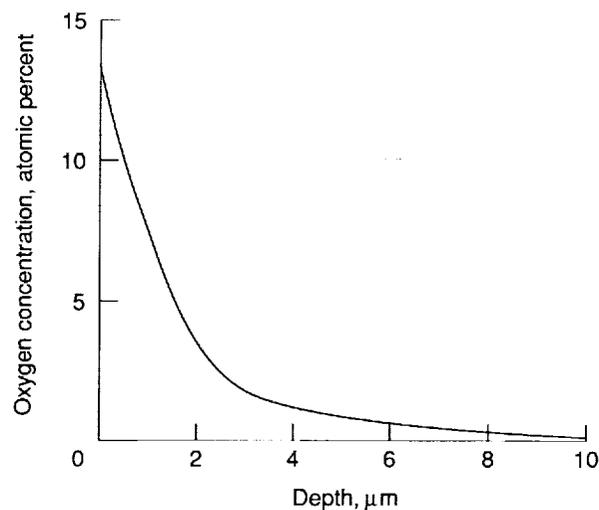

Figure 11. Oxygen depth profile computed from XRD data of Ti-14Al-21Nb alloy after exposure at $649°C$ for 112 hr.
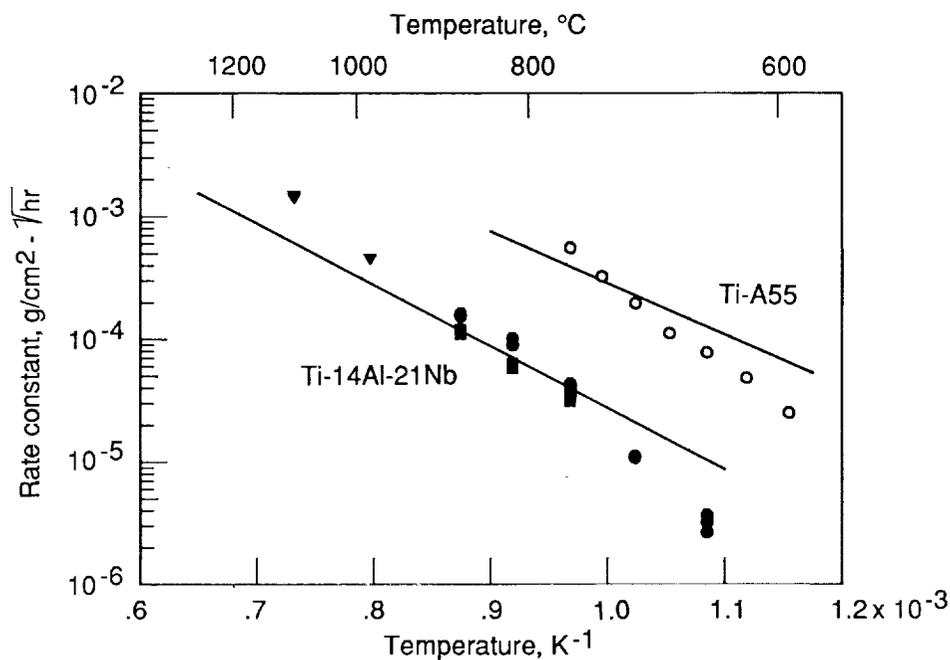
Figure 12. Comparison of measured and predicted oxidation rate constants for Ti-14Al-21Nb alloy and Ti-A55. Symbols are experimental points from figure 4 and solid lines are from theoretical estimation.
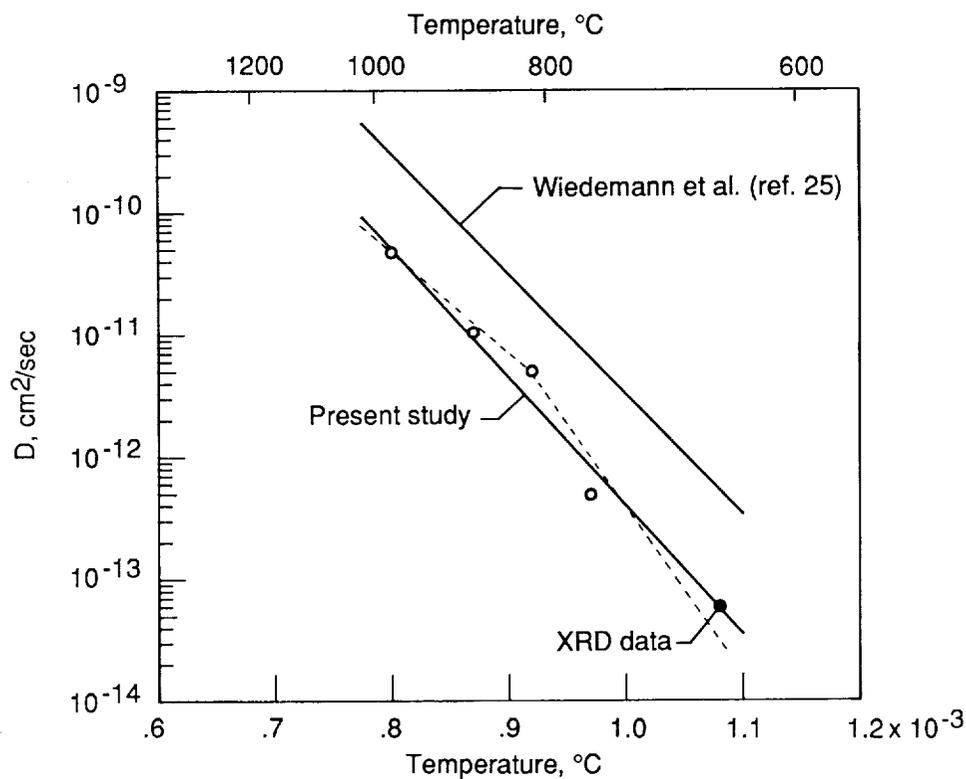

Figure 13. Comparison of oxygen diffusivity in Ti-14Al-21Nb alloy measured from the present study and the XRD data. Dashed line represents an alternate fit of the data. Diffusion coefficient (D) of the present study was $0.013 \ \mathrm{cm^2/sec} \ \exp\left(\dfrac{48\,100 \ \mathrm{cal/mol-K}}{RT}\right)$.

NASA
National Aeronautics and Space Administration

Report Documentation Page

1. Report No. NASA TP-3012	2. Government Accession No.	3. Recipient's Catalog No.
4. Title and Subtitle Oxidation Characteristics of Ti-14Al-21Nb Alloy		5. Report Date July 1990
		6. Performing Organization Code
7. Author(s) Sankara N. Sankaran, Ronald K. Clark, Jalaiah Unnam , and Karl E. Wiedemann		8. Performing Organization Report No. L-16658
9. Performing Organization Name and Address NASA Langley Research Center Hampton, VA 23665-5225		10. Work Unit No. 505-43-71-01
		11. Contract or Grant No.
12. Sponsoring Agency Name and Address National Aeronautics and Space Administration Washington, DC 20546-0001		13. Type of Report and Period Covered Technical Paper
		14. Sponsoring Agency Code

15. Supplementary Notes

Sankara N. Sankaran, Jalaiah Unnam, and Karl E. Wiedemann: Analytical Services & Materials, Inc., Hampton, Virginia.
Ronald K. Clark: Langley Research Center, Hampton, Virginia.

16. Abstract

The static oxidation kinetics of Ti-14Al-21Nb (percent weight) ingot alloy were studied in air over the temperature range from 649°C to 1093°C in a thermogravimetric apparatus. The oxidation products were characterized by X-ray diffraction, electron microprobe analysis, energy dispersive X-ray analysis, and Auger electron spectroscopy. Cross sections of the oxidized samples were also examined using light and scanning electron microscopy. The oxidation rate was substantially lower than the conventional alloys of titanium, but the kinetics displayed a complex behavior involving two or more oxidation rates depending on the temperature and duration of exposure. The primary oxide formed was TiO_2, but this oxide was doped with Nb. Small amounts of Al_2O_3 and TiN were also present in the scale. The diffusion of oxygen into the alloy was observed, and the diffusivity seemed to be dependent on the microstructure of the metal. A model has been presented to explain the oxidation behavior of the alloy in terms of the reduction in the oxygen diffusivity in the oxide caused by the modification of the defect structure of TiO_2 by Nb ions.

17. Key Words (Suggested by Authors(s)) Oxidation Oxidation kinetics Titanium-aluminide alloys	18. Distribution Statement Unclassified—Unlimited Subject Category 26		
19. Security Classif. (of this report) Unclassified	20. Security Classif. (of this page) Unclassified	21. No. of Pages 22	22. Price A03